Spikes matter for phase-locked bursting in inhibitory neurons

Sajiya Jalil, Igor Belykh, and Andrey Shilnikov

Department of Mathematics and Statistics, Georgia State University, 30 Pryor Street, Atlanta, Georgia 30303, USA and
Neuroscience Institute, Georgia State University, 100 Piedmont Street NW, Atlanta, Georgia 30303, USA

We show that inhibitory networks composed of two endogenously bursting neurons can robustly display several coexistent phase-locked states in addition to stable antiphase and in-phase bursting. This work complements and enhances our recent result [Jalil, Belykh, and Shilnikov, Phys. Rev. E **81**, 045201(R) (2010)] that fast reciprocal inhibition can synchronize bursting neurons due to spike interactions. We reveal the role of spikes in generating multiple phase-locked states and demonstrate that this multistability is generic by analyzing diverse models of bursting networks with various fast inhibitory synapses; the individual cell models include the reduced leech heart interneuron, the Sherman model for pancreatic beta cells, and the Purkinje neuron model.

I. INTRODUCTION

Phase locking between oscillatory cells plays a significant role in functions of various regulatory and nervous systems such as vision and memory [1]. These, and many other, systems are controlled by central pattern generators (CPGs) [2–5]. CPGs are small neuronal networks that generate various phase-locked bursting rhythms, including cardiac beating and locomotor behaviors [3]. The advancement of electrophysiological tools and methods has allowed biophysical properties of several CPGs and their component neurons to be identified and studied [3,6,7]. CPGs of many animals are composed of pairs of reciprocally inhibiting neurons. These universal pairs, often referred to as half-center oscillators, typically produce alternating, or antiphase, bursting rhythms. They can also produce less robust in-phase bursting when driven externally or endogenously [11].

The original concept of the half-center oscillator was proposed by Brown in 1911 [5] while studying animal locomotor behaviors and their associated neuronal rhythms. Brown proposed that antiphase bursting in the classical half-center oscillator (HCO) [5] is due to interactions between individually spiking (nonbursting) neurons. In this paper, the HCO is viewed more broadly as a reciprocally inhibitory, two-neuron configuration that can produce antiphase bursting. There have been many studies of mechanisms that generate bursting in individual and networked neurons, including transitions to bursting, tonic spiking, or quiescence [8–10,12–14].

Interactions between neurons in CPG networks are highly nonlinear and nonhomogeneous as the neurons receive uncorrelated driving inputs from each other at the same time. Nevertheless, the stunning feature of all CPGs is the robust and stable timing in their oscillatory rhythms [4]. There are several aspects to consider when seeking explanations for this generic and noticeable CPG phenomenon. These aspects include properties of individual neurons or neuronal models, types, and time scales of synaptic coupling, as well as network architectures of CPGs (see [2,11,12,15–36]) and the references therein. The mechanisms that give rise to antiphase bursting in the HCO have been under particular scrutiny [2,15]. Some of the mechanisms are synaptic release, post-inhibitory rebound, and synaptic escape mechanisms [2]. Reciprocal inhibition has been shown to facilitate antiphase bursting in the HCOs

[2,15,16,25,34] as long as the inhibition stays fast [16,19,22], meaning the synaptic decay is on the time scale of a single spike. Rubin and Terman demonstrated that synchronous oscillations are unstable in an HCO composed of fast inhibitory spiking (nonbursting) cells [19,22], unless each cell has at least two slow intrinsic variables [21]. In a seminal paper [16], van Vreeswijk, Abbott, and Ermentrout showed that the noninstantaneous "inhibition, not excitation, synchronizes" oscillatory neurons, resulting in simultaneous spike firing. Another possible mechanism of the stable coexistence of in-phase and antiphase bursting in the HCO is due to time-delayed synapses [15].

In our recent Rapid Communication [35], we demonstrated that the fast nondelayed reciprocal inhibition can stably synchronize endogenously bursting cells in the HCO due to spike interactions during the active phase. Fast inhibition is typical in many neuronal networks such as the leech heartbeat CPG [37] and the Tritonia swim CPG [38]. The bistability in HCO networks can make the CPG multistable with a bursting repertoire of two (antiphase and in-phase) or more complex rhythms [36]. Such HCOs with bursting neurons contrast with the HCOs comprised of relaxation-type cells, which are only capable of generating a single antiphase rhythm. Less robust compared to antiphase bursting, in-phase bursting can be effectively established in the HCO after both cells have received an external inhibition from another bursting neuron [11,12]. Our previous study [35] indicated the significance of spike interactions for establishing synchrony in fast inhibitory networks.

In this paper, we revisit the HCOs composed of square-wave bursters in order to examine a more general property of the coupled neurons: the coexistence of multiple phase-locked states. This coexistence results in the occurrence of specific phase lags or time delays between the nearest intervals of spiking or active phases in voltage traces. To the best of our knowledge, this phenomenon for realistic fast synapses has not been reported elsewhere. Multiple phase-locked states, however, were reported in several cases of slow inhibitory [15,16] and fast excitatory synapses [17]. We assert that multistability is a common phenomenon for square-wave bursting neurons coupled reciprocally by fast inhibitory synapses. To justify this assertion, we analyze diverse models of square-wave

bursting neurons such as leech heart interneurons [9,10], Sherman pancreatic beta cells [18], Purkinje neurons [13], and consider a few models of fast nondelayed inhibitory synapses. This analysis reveals the general ability of such HCOs to produce multiple coexistent phase-locked bursting patterns. We demonstrate that the number of phase-locked states is essentially determined by the number of spikes in the burst. These results may not hold for weakly coupled elliptic bursters, the formation of which involves delayed loss of stability and canard solutions [29]. As a result, the number of generated spikes may vary irregularly and the HCOs composed of elliptic bursters might not consistently have stable multiple phase-locking states.

Our computational approach enhances the perturbation technique of phase resetting curves (PRCs) [27]. The conventional PRCs are proved to be an effective tool for analyzing spiking neuronal models and allow for analytical analysis at some degree. However, the PRC technique, in application to bursting cells interacting during the active phase, has turned out to produce rather complex outcomes (due to highly timing-sensitive changes in the number of spikes per burst that can sporadically cause large magnitude phase responses) even in the weak coupling case [39]. We argue that the stability diagrams, along with Poincaré return mappings based on the variations of phase lags between the neurons, are a more efficient tool for thorough studies of spike interactions during active phases of bursting.

The layout of this paper is as follows. In Sec. II, we introduce the HCO concept employed in this study and describe the models of the neurons and synapses. In Sec. III, we present weakly coupled HCOs, as well as the methods and materials used to explore phase-locked states, namely, the way the phase of a bursting cycle is defined for examinations of coexistent phase-locked states. Next, we explain how inhibition and spike interactions induce stable phase-locked states. We measure these spike interactions and construct stability diagrams for phase lags between bursts produced by each coupled neuron. We introduce an effective potential to quantify the stability of phase-locked states, through the depths of wells, which correspond to stable states. Finally, we analyze and compare HCOs, made of square-wave bursters, using Poincaré mappings for phase lags, the fixed points of which correspond to phase-locked states. In Sec. IV, we study the stability of in-phase bursting in strongly coupled HCOs. The models employed in this study are presented in the Appendix.

II. NETWORK MODEL

We model a HCO network by means of Hodgkin-Huxley–type equations

$$CV_i' = F(V_i, \mathbf{h}_i) - I_{\text{syn}}^{(ij)}, \quad \tau(V_i)\mathbf{h}_i' = G(V_i, \mathbf{h}_i), \quad i,j = 1,2 \tag{1}$$

where V_i stands for the ith neuron membrane potential, and $\mathbf{h}_i$ stands for the gating (in)activation variable(s) describing kinetics of specific ion current(s) with a characteristic time scale(s) $\tau(V)$. Neurons composing the HCO are assumed to be identical. The individual neuron models we use are (i) the three-dimensional (3D) reduced model of the leech heart interneuron [9,10]; (ii) Sherman β-cell model [18]; and

(iii) the five-dimensional (5D) single compartment Purkinje neuron model [13]. All three models (see Appendix) are referred to as square-wave bursters, named for the resemblance of the shape of the envelope of bursts in the voltage traces [8].

The inhibitory synaptic current $I_{\text{syn}}^{(ij)}$ from the presynaptic cell j, flowing into the postsynaptic cell i, is recast as follows:

$$I_{\text{syn}}^{(ij)} = g_{\text{syn}}^{(ij)}(V_i - E_{\text{syn}})S(V_j), \tag{2}$$

where $g_{\text{syn}}^{(ij)}$ is the maximal conductance of the synapse. In other words, the maximum possible strength of the synaptic coupling from presynaptic neuron j to postsynaptic neuron i is given by $g_{\text{syn}}^{(ij)}$. Unless stated otherwise, the connections are assumed to be symmetric such that $g_{\text{syn}}^{(ij)} = g_{\text{syn}}^{(ji)} = g_{\text{syn}}$. The reversal potential is set so that $E_{\text{syn}} < V_i(t)$ at all times t to ensure the inhibitory nature of the current. Specifically, $E_{\text{syn}} = -0.0625$ V is fixed for the leech heart interneuron model, and $E_{\text{syn}} = -0.08$ V is set for the Sherman β-cell and Purkinje cell models. In this study, we employ four distinct models of the synaptic function $S(V_j)$, representing fast nondelayed synapses. Multiple phase-locked states turned out to be a common feature of HCO networks regardless of any particular choice of $S(V_j)$ considered in this paper.

(i) *Heaviside synapse.* This is the simplest representation of the synapses [17,21]: $S(V_j) = H(V_j - \Theta_{\text{syn}})$ with $H = \{0,1\}$. The synapse activates instantaneously, $S(V_j) = 1$, as soon as the membrane potential V_j of the presynaptic neuron exceeds the synaptic threshold Θ_{syn}, and deactivates instantaneously, $S(V_j) = 0$, after V_j drops below Θ_{syn}. The synaptic threshold Θ_{syn} is chosen to ensure that every spike of the bursting cell crosses the threshold [Fig. 1(a)]. The actual value for Θ_{syn} is determined for each model individually. Unless specified otherwise, we fixed $\Theta_{\text{syn}} = -0.0225$ V for the leech heart interneuron model, $\Theta_{\text{syn}} = -0.03$ V for the Sherman model, and $\Theta_{\text{syn}} = -0.036$ V for the Purkinje cell model.
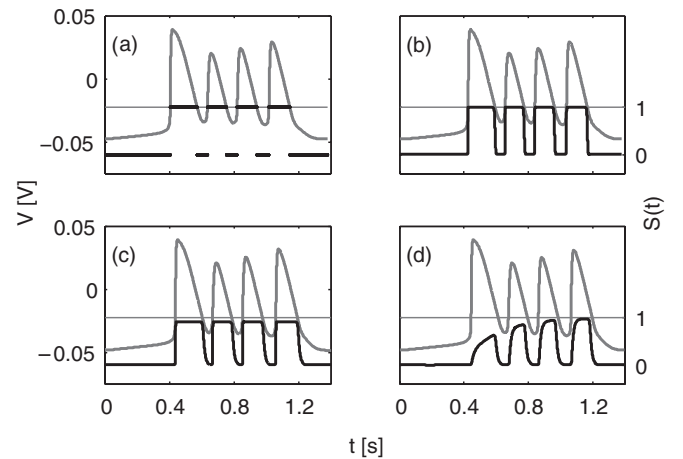

FIG. 1. Four-spikes bursting in the leech heart interneuron HCO (A1). Overlaid is the normalized synaptic function $S(t)$ for the synapse at the threshold $\Theta_{\text{syn}} = -0.0225$ and maximal conductance $g_{\text{syn}} = 0.005$ and modeled by the (a) Heaviside function; (b) FTM coupling; (c) α synapse; and (d) leech heart dynamical synapse.

(ii) *Fast threshold modulatory (FTM) synapse.* The coupling function is modeled by the sigmoidal

$$S(V_j) = 1/\{1 + \exp[-1000(V_j - \Theta_{\text{syn}})]\}. \quad (3)$$

This coupling form was introduced and called the fast threshold modulation by Somers and Kopell [17]. It is a smooth version of the Heaviside coupling function with the same rise and decay times [compare Figs. 1(a) and 1(b)]. The FTM is a remarkable model of a realistic fast synapse [17,21], such as that in the leech heart CPG [37], as it yields a nearly instantaneous response from the synapse on the postsynaptic neuron.

(iii) α-*dynamical synapse.* In this frequently used model of the synapse [15,16], the coupling function $S(V_j)$ is described by the following ordinary differential equation (ODE):

$$S'(V_j) = \alpha(1 - S)\{1 + \exp[-1000(V_j - \Theta_{\text{syn}})]\}^{-1} - \beta S. \quad (4)$$

Here, $\alpha = 1000$ and $\beta = 100$ are set to match the rate of the synaptic onset, decay, and maximum efficacy ($S \approx 1$) similar to the FTM synapse [see Fig. 1(c)]. Decreasing β causes the synaptic current to last longer.

(iv) *Leech heart dynamical synapse.* The last model for fast synapses is from the leech heart CPG, introduced in Ref. [37], where $S(V_j) = YM(V_j)$ is such that the fitted dynamics of the variables Y and M are governed by the auxiliary ODE system:

$$\dot{X} = (\{1 + \exp[-1000(V_j - \Theta_{\text{syn}})]\}^{-1} - X)/0.002,$$
$$\dot{Y} = (X - Y)/0.011,$$
$$\dot{M} = (0.1 + 0.9\{1 + \exp[-1000(V_j + 0.04)]\}^{-1} - M)/0.2. \quad (5)$$

We conclude this section with the remark that despite quantitative disparities due to the renormalization, all four models of the fast synapses consistently demonstrate homogeneous outcomes for all three neuron models of bursters in the HCO network. Moreover, we notice that the last model, which is experiment based [37], demonstrates fast decay of synaptic gating variable $S(t)$, such that inhibition is completely turned off between spikes in the burst, a phenomenon captured also by the other models of nearly instantaneous synapses. However, many physiological synapses have a slower rate of neurotransmitter dynamics than that of the channels, generally referred to as the slow synapses. As a result, such synapses slowly decay when the voltage in the presynaptic neuron falls below the synaptic threshold, causing summation of the synaptic current during a burst. Our results do not directly carry over to the slow synapses and are limited to the fast synapses, the decay of which is comparable to the duration of presynaptic drive.

III. WEAKLY COUPLED HCO: MULTIPLE PHASE-LOCKED STATES

A. Phase definition and phase locking

We begin with the HCO (1) composed of the leech heart interneurons (A1) coupled by weak FTM inhibitory connections (3). We reported earlier [35] that this HCO bursts, not only in antiphase as predicted and generally accepted, but
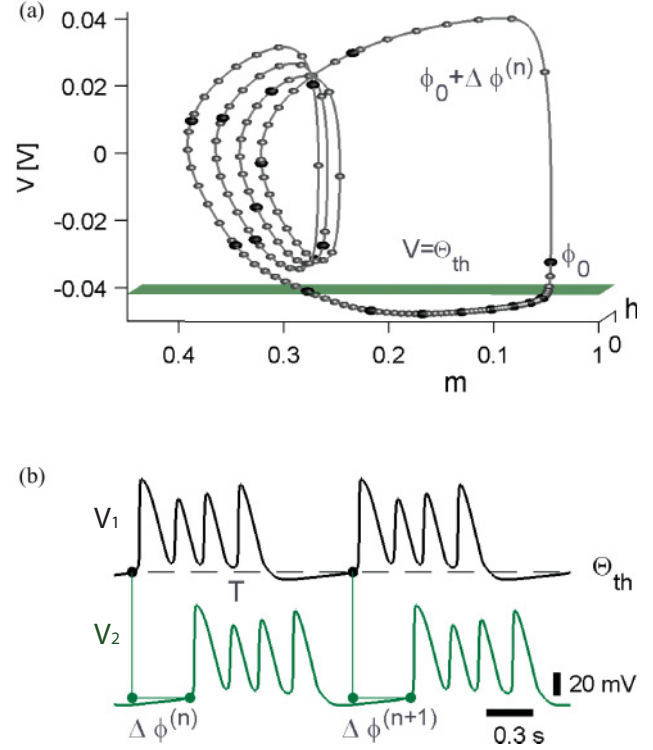

FIG. 2. (Color online) (a) Periodic bursting orbit in a 3D projection of the phase space of the leech heart HCO. Dark and lighter spheres represent, schematically, the densely distributed initial phases ϕ_0 for neuron 1 (reference) and $\phi_0 + \Delta\phi^{(0)}$ for neuron 2 across the bursting orbit of a normalized 1-period. (b) The sequence $\{\Delta\phi^{(n)}\}$ for every initial phase lag $\Delta\phi^{(0)}$ (out of 7 200) is identified from the traces at the instances when the ascending voltage $V_{1,2}$ passes through an auxiliary threshold Θ_{th} shown in (a).

it also stably bursts in phase. We will show that the weakly coupled HCO possesses multiple, coexistent phase-locked states, in addition to in-phase and antiphase bursting. Then, we demonstrate that the coexistence of several phase-locked states is due to spike interactions in overlapping bursts. To do so, we first introduce the phase and phase lag of the periodic bursting orbit.

The algorithm for identifying phase lags between the bursting neurons of the HCO is based on the observation that solutions of the two individual neurons of the HCO belong to the same orbit, therefore pass through a reference point in the phase space with some delay. We set the reference point to be on the auxiliary threshold $\Theta_{\text{th}} = -0.0425$ V [see Fig. 2(a)], halfway between the spiking and quiescent voltage values. The phase of the bursting neuron is initiated and reset every cycle after the voltage $V(t)$ increases above Θ_{th}. The phase lag $\Delta\phi^{(n)}$ on the nth bursting cycle is defined through the delay τ_n between the burst initiations $V_1(t_n) = \Theta_{\text{th}}$ and $V_2(t_n + \tau_n) = \Theta_{\text{th}}$ [see Fig. 2(b)], which is further normalized over the recurrence period $T^{(n)} = t^{(n)} - t^{(n-1)}$ of the HCO. A detailed account of the routine for the computations of the sequence $\{\Delta\phi^{(n)} = \tau^{(n)}/T^{(n)}\}$ is given in Ref. [36].

We consider the case of the weak inhibitory coupling $g_{\text{syn}} = 0.005$ between the neurons in the HCO. Such weak coupling does not drastically change the phase lags $\Delta\phi^{(n)}$
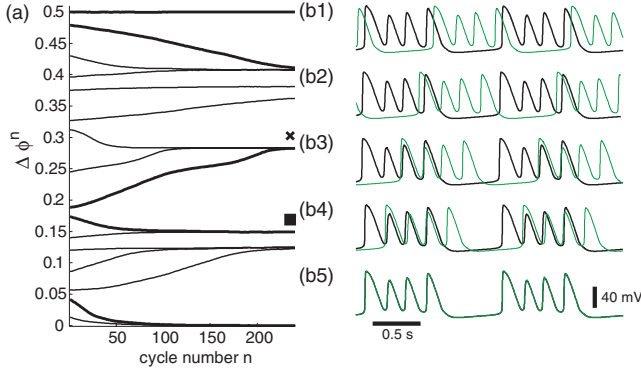
FIG. 3. (Color online) (a) Exponential convergence of initial phase lags to four coexistent phase-locked states over 200 burst cycles of the leech heart HCO. Parameters are $\Theta_{\text{syn}} = -0.0225$, $V_{\text{K2}}^{\text{shift}} = -0.022$, and $g_{\text{syn}} = 0.005$. $\Delta\phi^{(n)} = 0$ and 0.5 correspond to stable in-phase and unstable antiphase bursting, respectively. The right panel shows the established bursting cycles (dark and light green colors for neurons 1 and 2, respectively) corresponding to the selected phase-locked states [thick lines in (a)]. Symbols $\times$ and $\blacksquare$ are the same in Figs. 4(c) and 4(d).

between the neurons over a bursting cycle thereby allowing us to follow "continuous" evolution of the phase lags $\Delta\phi^{(n)}$ as the number n of bursting cycle progresses. A word of caution: such continuous evolution may be hard to achieve when the individual neuron is defined by parameters close to a bifurcation such as the one underlying slow transition from bursting to tonic spiking or quiescence. Slow evolution of the phase lags, however, lets us systematically single out all coexisting stable phase-locked states and identify the separating thresholds (unstable states), as we evaluate the convergence rates given by $\Delta\phi^{(n+1)} - \Delta\phi^{(n)}$. Figure 3(a) represents the evolution of the phase lags $\Delta\phi^{(n)}$ plotted against the number of burst cycles n for the leech heart HCO generating four spikes per burst. By assessing convergent tendencies of $\Delta\phi^{(n)}$, as n increases, in the figure one can clearly identify four stable phase-locked states (nonlinear thick curves), which include the synchronous state $\Delta\phi^{(n)} = 0$. Unstable states are invisible, but they exist between every pair of stable states. We see four unstable states, which include the antiphase state $\Delta\phi^{(n)} = 0.5$ (constant thick curve). Figure 3(b) depicts the voltage traces for bursting patterns corresponding to the states: antiphase (b1) through in phase (b5). In what follows, we give an explanation for causes of these multistable states.

B. Mechanism of multistability: Two opposite roles of inhibition

In this section, we argue that the cause of multistability is a dual role of inhibition. Since the periodic orbit does not significantly deform the shape in the limiting case of the uncoupled network, motion along the orbit is integrative, that is, displacement due to action of synaptic current, normal to the orbit, adds up along the trajectory. However, due to the oscillatory nature of spiking, the inhibition from a presynaptic neuron can either speed up (add to) the postsynaptic neuron on the downstroke (decreasing further $V' < 0$) or slow it down (subtract) on the upstroke (decreasing $V' > 0$) as one can see from the modeling equations (1). Because the inhibition
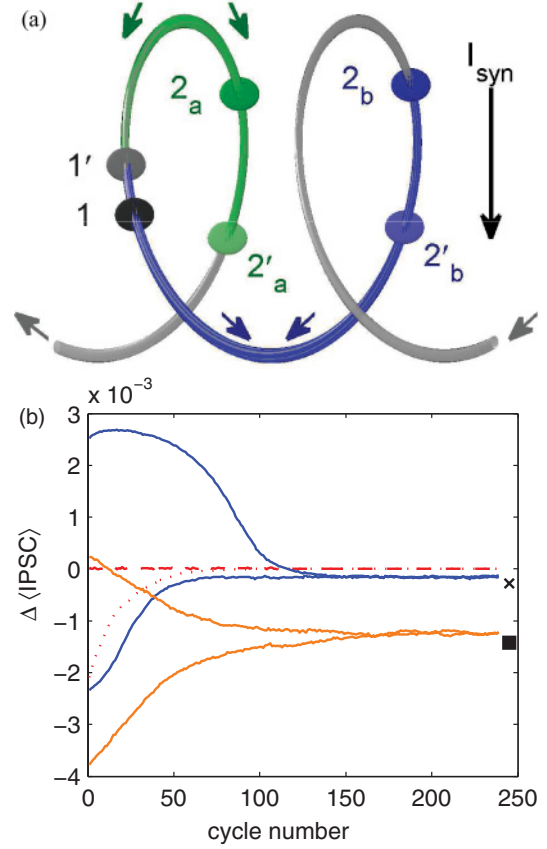

FIG. 4. (Color online) (a) Illustration of the dual, slowing and speeding, roles of reciprocal inhibition on evolution of the phase lags during the spiking phase on the bursting orbit, sketched as a helix segment in $\mathbf{R}^3$ with the voltage on the vertical axes. Spheres $1,1'$ denote the reference neuron 1 on the upstroke, while spheres $2_a,2'_a,2_b,2'_b$ denote the instant phases of the neuron 2 on downstrokes. Arrows indicate the direction of inhibition at the current phases of the neurons that make the phase lags widen (upper arch between 1 and 2_a) or narrow (low arch between 1 and 2_b) along the bursting orbit. (b) Transients of the averaged net synaptic current $\Delta\langle\text{IPSC}\rangle$ converging to two nonzero equilibrium levels representing the (b3:$\times$) and (b4:$\blacksquare$) phase-locked states. Transients converging to the zero level for the stable in-phase (dotted line) phase-locked state, as well as unstable antiphase state (dashed line).

is reciprocal in the HCO, this argument also applies to the other neuron. As a result, depending on timing, the phase lag between the neurons can shrink or widen during the spiking period of bursting, thereby giving rise to multiple phase-locked states. The mechanism is illustrated in Fig. 4(a), depicting the momentary phases of the reference neuron 1 on the upstroke (above the synaptic threshold) and the two relative positions of neuron 2 both on the downstroke along the bursting orbit in the active, spiking phase. In the first case, the initial distance (upper arch of the spiking helix) or the phase lag between neurons 1 and 2_a widens because the phase $1'$ is slowed on the upstroke by inhibition from the neuron 2_a, while the phase $2'_a$ is accelerated on the downstroke due to the reciprocation from the neuron 1. In the second case, the reciprocal inhibition makes the distance (low arch) between the neurons 1 and 2_b shrink instead, thus narrowing the phase lag (arch between $1'$ and $2'_b$)

with each cycle. Note that during simultaneous upstrokes and downstrokes, discrepancies in inhibition are less significant. The overall cells' convergence to or divergence from the given phase-locked state depends on the initial conditions that in turn define a fragile balance between the two competing, slowing and speeding, forces over the bursting period. The above mechanism is dependent on the assumption of weak coupling where nonintegrative motion that is not tangential to the cycle can be neglected.

An average effect of instantaneous spike interactions on phase lags per burst cycle can be assessed from Fig. 4(b), showing the dynamics of the net synaptic current $\Delta \text{IPSC} = I_{\text{syn}}^{(12)} - I_{\text{syn}}^{(21)}$ for several initial phase lags. The vertical axis represents the difference between the average synaptic currents $\Delta \langle \text{IPSC} \rangle$ generated by both neurons. The figure shows that $\Delta \langle \text{IPSC} \rangle$ settles down to a constant value after a number n of bursting cycles when a phase-locked state is achieved. The rate of change of $\Delta \langle \text{IPSC} \rangle$ approaches zero when all spikes with a burst are aligned. The attracting phase-locked states are represented by the horizonal lines indicating the levels of $\Delta \langle \text{IPSC} \rangle$ on established HCO configurations. While the zero level corresponds to two opposite states, unstable antiphase and stable in-phase bursting with four spikes, nonzero states correspond to other configurations such as Figs. 3(b3) and 3(b4) spike offsets marked by $\times$ and $\blacksquare$. This presents a very peculiar observation that overlapping bursting can generate nonzero amounts of average net inhibition for phase-locked states to maintain (locally) the stability, even forcibly, that gives rise to the nonlocal multistability of the HCO.

To conclude, we emphasize the ability of inhibition to speed up or slow down depending on whether the driven postsynaptic neuron is on the downstroke or upstroke, respectively. Note that the neurons become decoupled during the spiking phase as soon as the voltage drops below the synaptic threshold. When the spikes are aligned, the relative phases speed up and slow down simultaneously, thus causing small variations in the phase lag. As a result, a weak coupling and a high synaptic threshold combined can give rise to the occurrence of multiple phase-locked states. This property is uniquely attributed to bursting cells with spikes as opposed to relaxation oscillator-type neurons without fast spikes that are capable of producing only antiphase bursting.

C. Stability diagrams

To analyze and quantify the stability of the phase-locked states (Fig. 3), we employ 1D stability diagrams (shown in Fig. 5) representing snapshots of the nth iterate of the difference between the current and preceding phase lags, i.e., $[\Delta \phi^{(n+1)} - \Delta \phi^{(n)}]$, plotted against the initial distribution $0 \leqslant \Delta \phi \leqslant 0.5$. For dense enough initial distribution, n can be taken as small as 2, which would give a scalar number corresponding to every initial phase lag. Observe that $[\Delta \phi^{(n+1)} - \Delta \phi^{(n)}]$ can also be viewed as the change rate over a single burst cycle on the nth step. If the change rate does not vary for some initial phase lag $\Delta \phi^*$, then the latter corresponds to a fixed point of the iterative process. A zero of the graph $[\Delta \phi^{(n+1)} - \Delta \phi^{(n)}]$ versus $\Delta \phi$ is a fixed point. The stability of the point is determined by the derivative $d[\Delta \phi^{(n+1)} - \Delta \phi^{(n)}]/d\Delta \phi$ at $\Delta \phi^*$. The fixed point is stable
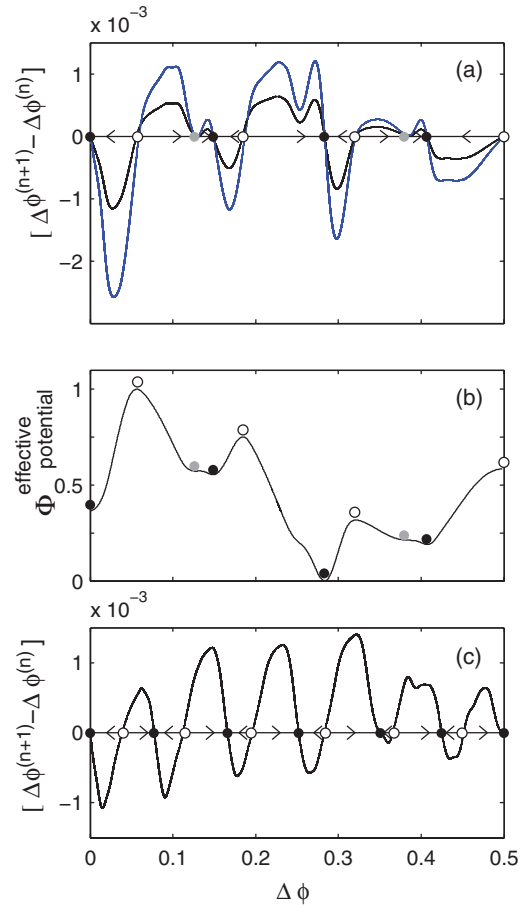

FIG. 5. (Color online) (a) Two graphs (black and blue/gray) of the 1D stability diagram: zeros of the stationary distribution of the phase lag difference $[\Delta \phi^{(n+1)} - \Delta \phi^{(n)}]$ over the range $\Delta \phi = [0, 0.5]$ are phase-locked states: four stable (solid dark circles) separated by repellers in the four-spikes bursting HCO at $V_{\text{K2}}^{\text{shift}} = -0.022$ at $g_{\text{syn}} = 0.005$ and $g_{\text{syn}} = 0.01$, respectively. (b) Normalized effective potential (integral) for $g_{\text{syn}} = 0.005$: different wells implying uneven robustness of the stable phase-locked states, the basins of which are separated by the thresholds. Solid gray circles indicate intermediate (saddle-node) states. (c) Zeros indicated by solid circles corresponding to seven stable phase-locked states, in the eight-spikes bursting HCO at $V_{\text{K2}}^{\text{shift}} = -0.024$, in the 1D stability diagram.

if the derivative is negative, or unstable if the derivative is positive. The basins of the stable states (four total as in Fig. 3) of the HCO network are separated by the unstable ones in this 1D phase portrait. Figure 5(a) shows the two 1D phase portraits of the leech heart HCO with a weak $g_{\text{syn}} = 0.005$ (black graph) and a stronger $g_{\text{syn}} = 0.01$ (blue/gray graph) coupling. In both cases, the fixed points are located at the same zeros of the graph of $[\Delta \phi^{(n+1)} - \Delta \phi^{(n)}]$. However, local (in)stability of the fixed point becomes quantitatively stronger with an increased coupling strength.

In addition to local stability, the robustness of the stable phase-locked states can be characterized in terms of an effective potential, which is a normalized integral numerically evaluated from the stability diagram in Fig. 5(a), and is given by the formula $\sum_{\Delta \phi=0}^{\Delta \phi} (\Delta \phi^{(n+1)} - \Delta \phi^{(n)}) / \sum_{\Delta \phi=0}^{0.5} (\Delta \phi^{(n+1)} - \Delta \phi^{(n)})$. In Fig. 5(b), the normalized effective potential plotted
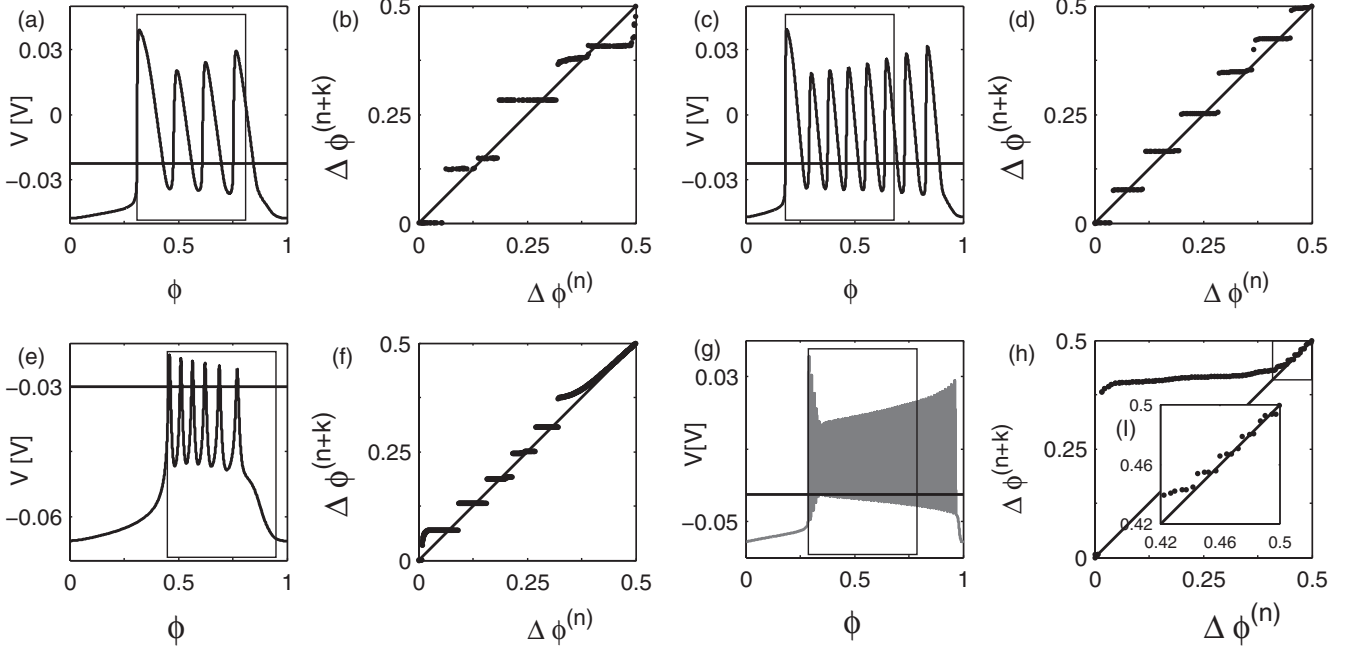
FIG. 6. Bursting cycles generated by the HCO composed of the leech heart interneuron models (a), (c) and the Sherman models (e) and the Purkinje cell models (g). Overlaid boxes indicate the reference half-period frames defining the spikes that effectively determine the number of phase-locked states in the networks; the horizonal lines set the synaptic thresholds in the HCOs. (b), (d), (f), and (h) show the corresponding 1D return mappings: $\Delta\phi^{(n)} \rightarrow \Delta\phi^{(n+k)}$ of degree k ($k = 345, 40, 80$ and 35, respectively). (b) and (d): Four and seven stable fixed points in the mapping imply the coexistence of the same number of phase-locked states in the bursting leech heart HCOs ($g_s = 0.005$). (e), (f): The Sherman model HCO ($g_s = 0.001$) generating six-spike bursting possess the same number of stable fixed points in the mapping. (e) Zoom of the mapping (h) for the the Purkinje cell HCO ($g_s = 0.001$) generating 62-spike burst trains reveals multiple phase-locked states within $[0.4, 0.5]$ range accumulating to antiphase bursting.

against the phase lag distribution $\Delta\phi$ reveals the profile of the potential wells corresponding to the attraction basins of stable states, and the barriers corresponding to the unstable states in the leech HCO network. This diagram allows us to identify the most robust phase-locked state by differentiating the depth and width of the wells. Observe from this figure that the steepness of the potential well yields nonlocal rate of convergence to the phase-locked states. This figure also shows that fast convergence to the in-phase ($\Delta\phi^* = 0$) state does not make it the most robust, as its basin is not as deep as those of other stable phase-locked states.

The comparison of Figs. 5(a) and 5(b) with the corresponding four-spikes bursting trace [Fig. 6(a)] suggests that there is a (direct) correlation between the number of spikes per burst and the number of stable phase-locked states. To support the hypothesis, we present Fig. 5(c) showing a similar 1D stability diagram for the eight-spikes bursting trace [Fig. 6(c)]: now the leech HCO possesses seven attractors corresponding to the stable phase-locked states. The relation between number of spikes and that of phase locking is still consistent because there are only six spikes that fall in the range $0 \leqslant \Delta\phi \leqslant 0.5$ and the antiphase state is located at $\Delta\phi = 0.5$, which has switched stability.

The qualitative examination of the stability of the fixed points for the phase lags, together with the quantitative observation, lets us hypothesize that spikes do matter for the emergence of multiple phase-locked states. The number of spikes per burst does yield an estimate for the number

of phase-locked states. However, complexity of the spike interactions due to timing, and irregularities of the spike characteristics, slow convergence due to weak coupling and the sensitivity of the two-time scales bursting solutions may cause inaccuracies in some models. Moreover, multistability of weakly coupled HCO becomes harder to describe properly as the duty cycle becomes greater, resulting in a long burst train with a larger number of spikes [Figs. 6(g) and 6(h)]. Meanwhile, the attraction basins of the phase-locked states become narrower and less clearly identifiable, which means that the accurate numerical simulations would require unrealistically high resolution. We have presented the most tractable cases so far, and next will introduce an alternate way of thoroughly examining multistability in all the cases considered so far in this paper. This method reduces the problem of finding and characterizing stability of phase-locked states to studies of 1D Poincaré return mappings.

D. Phase return maps

Identifying multiple phase-locked states of the bursting HCO can effectively be reduced to that of finding stable fixed points in 1D Poincaré return mappings defined as $\Delta\phi^{(n)} \rightarrow \Delta\phi^{(n+k)}$, where k is the degree of the mapping. For a nonstationary phase lag, either $\Delta\phi^{(n+k)} > \Delta\phi^{(n)}$ or $\Delta\phi^{(n+k)} < \Delta\phi^{(n)}$ for $k = 1$, but the change is small because of the "continuity" condition mentioned earlier: the case of the weak coupling, which results in slow and smooth dependence

of $\Delta\phi^{(n)}$ on the burst cycle number n [Fig. 3(a)]. As a result, the slope of the mapping at a stable fixed point is $1 - \epsilon$ [for k-degree mapping the slope $(1 - \epsilon)^k \to 0$] and at an unstable fixed point it is $1 + \epsilon$ [k-degree slope $(1 + \epsilon)^k \to \infty$]. Hence, the integer k may be chosen relatively large for the basins of attractions to be well identified. Specific values of k depend on the individual cell model in question as they have distinct rates of the convergence to the phase-locked states. So, $(k - 1)$ is the number of successive burst cycles skipped in the traces to generate the mappings. By choosing the degree to be k, the mapping reveals robust phase-locked states that are represented by stable fixed points, located at intersection points of the flat sections (slope 0) of the mapping graph with a $45°$ line. Due to the large values of k, the unstable fixed points corresponding to the threshold separating the attraction basins reside at the discontinuity points (slope ∞) of the mapping graph.

Figure 6 presents four pairs of panels, each representing bursting rhythms and the corresponding return mappings for the four HCOs under consideration. Figures 6(a)–6(d) depict, respectively, the voltage traces and the mappings $\Delta\phi^{(n)} \to \Delta\phi^{(n+k)}$ of degrees $k = 345$ and 40 for the weakly coupled leech heart HCOs, which robustly produce four and eight spikes per bursting cycle. Figures 6(e)–6(h) are for the HCOs made of the Sherman pancreatic β-cell models and the Purkinje cell models, respectively. The frames overlaid on top of the bursting traces denote half-period windows, $0 \leqslant \phi \leqslant 0.5$, with the spikes determining the number of phase-locked states. By construction, the phase lag $\Delta\phi$ is symmetric about the half-period point such that the phase lags outside and inside of the half-period frame are equivalent. This implies that only the spikes within the frames are critical for spike interactions leading to phase-locked states.

Figure 6 suggests that the CPG models under consideration possess the same universal properties, which are due to spike interactions contributing to the emergence of multiple phase-locked states. There are some distinctions as well, for example, wide asymmetric spikes produced nonhomogeneously by the leech heart interneuron model can result in more subtle attraction basins and less robust phase-locked states, including metastable states near saddle-node equilibria (Fig. 6) or tangent fixed points (Fig. 6). Those metastates have vanished, and phase-locked states gain robustness, as the number of spikes per burst becomes larger. Furthermore, narrow symmetric spikes produced evenly by the bursting Sherman model HCO contribute to the occurrence of robust phase-locked states with well defined (separated) basins of attraction [see Figs. 6(e) and 6(f)]. Remarkably, the number of the spikes occurring within the half-period windows in the leech heart and Sherman β-cell HCOs accurately determines the number of coexisting stable phase-locked states.

The Purkinje model generates long bursts with multiple, nearly instantaneous spikes at the chosen parameter values. Because of that, it is hard to identify a large number of all phase-locked states with rather narrow attraction basins in the weakly coupled ($g_{syn} = 0.001$) HCO case due to slow convergence. To take fewer spikes into consideration, we lowered the synaptic threshold Θ_{syn} so that spikes occurring closer to the end of the burst cycle can actually cross it [Fig. 6(g)]. As a result, the corresponding Poincaré map-

ping $\Delta\phi^{(n)} \to \Delta\phi^{(n+k)}$ (here $k = 80$) has an array of fixed points, within the range [0.4, 0.5] near the phase-locked state corresponding to antiphase bursting produced by the HCO. Additionally, this demonstrates the significance of the choice for the synaptic threshold in modeling studies of larger network models, such as specific central pattern generators that are often comprised of several HCOs.

To conclude this section of the paper, we point out that we have demonstrated how various intrinsic properties of the HCOs, including correlations between the number of spikes and the temporal characteristics of bursting, including the spike frequency, duration, and duty cycles, as well as the level of the synaptic threshold, all combined, may determine the number of coexisting phase-locked states. While the strength of the synaptic coupling modulates the amplitude of the synaptic current, and hence influences the spike interaction, our simulations suggest that variations of the coupling strength do not essentially influence the number of stable phase-locked states as long as the coupling remains weak, which in turn guarantees the relatively slow convergence to either phase-locked state. A significant increase in the coupling strength makes most phase-locked states disappear so that antiphase bursting will solely persist in the HCO, which is the general convention. In the next section, we show that in-phase bursting can also persist as stable, although comparably less robust, in strongly coupled HCOs.

IV. QUASI-STRONGLY COUPLED NETWORKS: STABLE IN-PHASE BURSTING

We define quasi-strong inhibition through coupling that is sufficiently strong to establish antiphase bursting rapidly, indicated by the convergence rate of the phase lags presented in the previous section. The rapid transitions appear as nonsmooth time evolution of phase lags leading to antiphase bursting. This occurrence precedes or coincides with the hold-then-release mechanism (due to a saddle-node bifurcation) [11], which happens to be functionally similar to synaptic release mechanism, common for relaxation oscillator-type spiking neurons [2,15,34]. The hold-then-release mechanism implies that the active presynaptic neurons temporarily lock down the inactive postsynaptic cell at the hyperpolarized state during the half-oscillator bursting cycle. Fast inhibition implies that as soon as the active neuron ceases firing and becomes inactive, the other cell is released from inhibition, so they switch roles to produce the second half-oscillator bursting cycle. This cyclic switching between active and inactive phases in the HCO gives rise to highly robust antiphase bursting. The details on emergent antiphase rhythms in HCOs made of bursting neurons can be found in Ref. [12] and the references therein.

Although it is possible for the HCO to establish in-phase synchrony coexisting with the antiphase synchrony induced by the hold-then-release mechanism, the attraction basin for in-phase synchrony tends to shrink with increased synaptic coupling. Previously [35], we considered a synapse to be strong as soon as the hold-then-release mechanism was able to engage. However, if the conventional definition of strong inhibition is assumed, then we have a quasi-strong coupling case, in which the in-phase synchrony has not completely lost

its stability, even though antiphase synchrony has emerged via the hold-then-release mechanism.

When the coupling is quasi-strong and the initial conditions of bursting cells are set so that one cell is active (above the synaptic threshold) while the other is inactive, then fast nondelayed reciprocal inhibition leads ultimately to antiphase bursting in any HCO, independent of the choice of models of individual bursters and fast synapses. Once achieved, antiphase bursting remains highly resistant to external voltage perturbations; however, this is not true when long (periodic) inhibition is forwarded to both cells from an external source. As shown in Ref. [11], this external inhibition establishes in-phase synchronization in the HCO.

In the previous section, we have stressed that the coexistence of multiple phase-locked states is a peculiar paradigm of the weakly, reciprocally inhibitory coupled HCO made of (nearly) identical cells. Increasing the coupling strength makes most, but not all, phase-locked states disappear eventually. Nevertheless, both weakly and quasi-strongly coupled HCOs exhibit antiphase bursting, generally, and the emergent mechanisms are different: a fragile balance between spike timing and IPSCs in the weak coupling case and the robust hold-then-release mechanism in the quasi-strong coupling case.

It is important to emphasize that the quasi-strong coupling considered in this section is far from being weak. In contrast to the classical weak coupling case where the periodic orbit of the coupled neuron does not differ significantly from that of the uncoupled neuron, the quasi-strong coupling can essentially change the dynamics of the coupled neuron. More precisely, the quasi-strong coupling, preserving coexistent in-phase and antiphase bursting, can generate extra spikes in the coupled square-wave bursting neuron.

A peculiar feature of the quasi-strong coupling is the robustness of in-phase bursting that coexists with antiphase bursting [35]. In-phase bursting emerges over a wide range of dispersed initial conditions chosen within the spiking phase of both cells. Initial conditions corresponding to the activity of one cell and inactivity of the other lead to the emergence of antiphase bursting via the above hold-then-release mechanism [11]. In Ref. [35], we demonstrated that the impact of inhibition on the bursting cells drastically depends on whether both cells are above the synaptic threshold Θ_{syn}. More specifically, we analyzed the variational equations for the stability of synchronized bursting and showed that inhibition instantaneously switches from desynchronization to synchronization as long as both cells become active. That is, if both bursting cells are initially active in the spiking phase of bursting, the inhibition, instead of desynchronizing them, will force the cells' states to come together, resulting in stable synchronized bursting.

The synchronizing effect of the fast inhibition is specifically due to spike interactions of the cells during the active phase of bursting. This property is linked to the presence of two competing, desynchronizing and synchronizing, synaptic terms in the variational equations [35]. That is, whenever one cell gets close to the threshold Θ_{syn}, the other cell receives a short-term desynchronizing kick that causes the divergence between the cells. However, when both cells rise above the threshold, the inhibition switches its role and the cells

converge. In this respect, inhibition acts as excitation during the time interval of simultaneous cell activity when both cells are above the synaptic threshold. This synchronization property of inhibitory bursting cells with spikes is in contrast with the HCO made of cells exhibiting spike-free relaxation-type bursting, such as plateau bursting where the fast inhibition carrying only desynchronizing effects makes stable synchrony impossible. More details on the mechanism of the inhibitory synchronization can be found in Ref. [35].

In this section, we demonstrate that in-phase bursting, coexisting with antiphase bursting, is a generic property of the HCO, composed of endogenously bursting (nearly identical) neurons, reciprocally coupled by fast nondelayed inhibitory synapses. This property is independent from the model of the fast nondelayed inhibition, be it the instantaneous Heaviside or FTM synapse or a dynamical synapse with the synaptic constants comparable with the duration of the presynaptic spike.

In what follows, we reveal the stability and robustness of in-phase bursting with respect to transversal perturbations against the phase mismatch (offset) between two neurons in the HCO. More specifically, we examine how the shape of the attraction basin of in-phase bursting varies along the in-phase bursting orbit. To do so, we first parametrize the bursting cycle with respect to a phase, defined on modulo 1, as described in the previous section. Next, the in-phase bursting cycle is
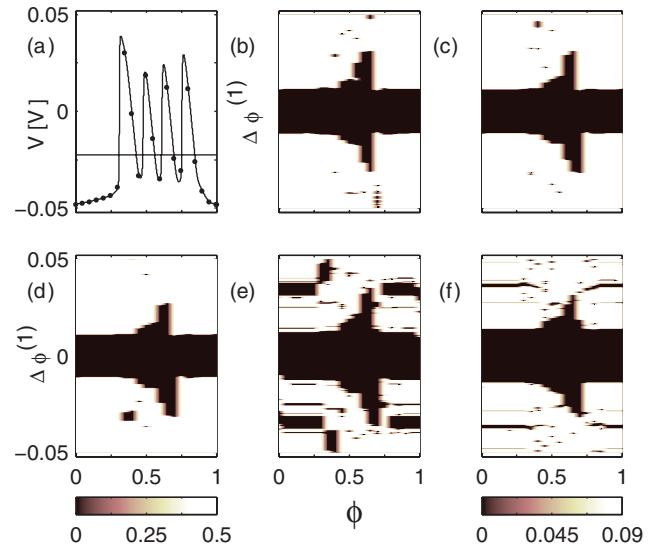

FIG. 7. (Color online) (a) Bursting cycle of the leech heart HCO at $g_s = 0.4$ is phase parametrized on the interval [0, 1]: dots indicate some reference phases used for identifying the attraction basins of in-phase bursting. The horizontal line across the spikes sets the level of the synaptic threshold $\Theta_{\text{syn}} = -0.0225$. Attraction basins of the in-phase state plotted against the phase along the bursting cycle for four models of inhibitory synapses: (b) Heaviside; (c) FTM coupling; (d) heterogeneous FTM coupling with $g_s^{(12)} = 0.4$ and $g_s^{(21)} = 0.44$; (e) α-dynamical synapse; (f) leech heart dynamical synapse. All cases reveal that the widest synchronization zone occurs during the tonic-spiking period of bursting, while quiescent period yields a narrow basin. In all panels, the range of $\Delta\phi$ is scaled between [−0.05, 0.05]. Color bars represent degree of phase synchrony (left) or spike synchrony (right).

discretized with a mesh, comprised of reference phase values [see Fig. 7(a)]. Each reference phase is employed to identify a local basin of attraction by gradually advancing, $\Delta\phi > 0$, or delaying, $\Delta\phi < 0$, the initial phase of the perturbed or the nonreference member of the HCO. In the remaining panels of Fig. 7, we plot the initial perturbations $\Delta\phi$ that resulted in spike and/or burst synchrony, against phase ϕ for the leech heart HCO with mutually inhibitory synapses described by the four models given in Sec. II.

The shaded regions in Figs. 7(b)–7(h) represent the largest deviation values of the phase perturbation $\Delta\phi$, and reveal that the width of the "synchronization band" varies with the phase; it is maximized during the active or spiking period, and shrinks during the quiescent period. For larger initial phase mismatches, the cells of the HCO will settle in antiphase bursting. Figure 7 also demonstrates that all selected models of inhibitory synapses agree, both quantitatively and qualitatively. Furthermore, as expected, longer lasting inhibitory inputs of the α-dynamical (4) and leech heart dynamical synapses (5) (cf. Fig. 1) ensure some wider synchronization zones. Indeed, beyond the critical values after which the synapse is considered slow or slowly decaying in time, antiphase bursting becomes nonobservable, thus leaving in-phase bursting as the only stable state; this is a classic result [16]. On the contrary, when synapses are fast, antiphase bursting largely dominates over much weaker in-phase bursting in the inhibitory HCOs (1). In-phase bursting necessarily requires close initial burst overlapping. Based on the analysis done in the previous section, we conclude that spike interactions bound the attraction basin of in-phase synchrony.

In addition to variations in the level of synaptic threshold Θ_{syn}, that of the synaptic strength g_{syn} is used to exam-ine the synchronization properties of in-phase bursting in quasi-strongly coupled HCOs. Figure 8 presents biparametric sweeping of (Θ_{syn}, g_{syn})-bifurcation diagram for in-phase bursting in the leech heart HCO with the four selected models of synapses. In the diagrams, shaded areas correspond to stability islands of in-phase bursting. For the given leech interneuron model, the synaptic coupling with g_{syn} exceeding 0.02 is considered quasi-strong as it leads right away to robust antiphase bursting via the hold-then-release mechanism [11]. Note that within the plausible range of values for the synaptic threshold $[-0.015, -0.005]$, the HCO possesses the largest stability islands where it can exhibit in-phase bursting. In this range, the synaptic threshold crosses the middle of all of the spikes, which ensures an optimal stabilizing balance for inhibiting synaptic currents to promote in-phase bursting. Lowering or raising the synaptic threshold out of this range makes in-phase bursting less robust, as the contribution of the spikes becomes less significant. After the synaptic threshold is lowered below the minimum voltage level of the spikes, the HCO cells begin bursting in antiphase, generally, similar to pairs of relaxation oscillators [2], such as Morris-Lecar or FitzHugh-Nagumo spiking neurons, where the spike interactions play no functional role.

V. CONCLUSIONS

We have shown that fast nondelayed inhibitory HCOs composed of two endogenously bursting neurons can generate multiple coexistent phase-locked states, in addition to stable antiphase and in-phase bursting. This is an extension of our previous result [35] that fast nondelayed reciprocal inhibition synchronizes HCOs, which contrasts with the customary view that reciprocal inhibition has to be slow or time delayed to establish in-phase bursting. We have shown that the multistability of the HCOs is due to spike interactions and independent of specific choice of models for endogenous square-wave bursters and fast nondelayed synapses. Fast tonic spiking and fast inhibition are the two necessary conditions for multistable bursting to exist in such HCOs. This is in contrast with plateaulike bursting, where spike interaction is insignificant because of the slow frequency and smoothed spiking magnitude relative to the plausible range of the synaptic threshold levels. We have shown that the number and temporal characteristics of spikes determine the number of coexisting phase-locked states in weakly coupled HCOs. Besides, spikes are also attributed to be the necessary component for dynamically establishing the bistability in quasi-strongly coupled HCOs, where robust antiphase bursting coexists with less robust in-phase bursting. This study emphasizes the importance of detailed Hodgkin-Huxley models for credible modeling of larger CPG networks, as opposed to employing relaxation oscillators, which might give rise to simplistic cooperative properties.

Our study of multiple phase locking in the HCOs and coexisting dynamical rhythms can help one better understand the origin of multistability and the nature of switching mechanisms between various neuronal rhythms that a multifunctional CPG can generate in response to changes in sensory inputs and external perturbation. Recent experimental studies [6] suggest that leech crawling and swimming can be generated by the
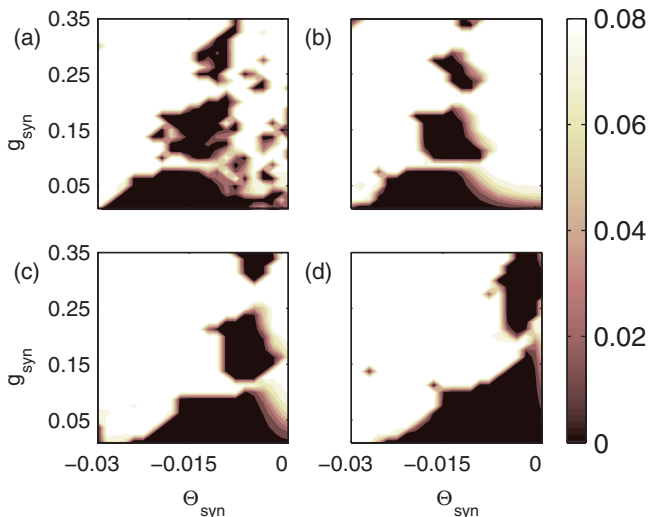

FIG. 8. (Color online) Biparametric (Θ_{syn}, g_{syn}) diagrams depicting stability zones (dark) of in-phase bursting in the leech heart HCO with inhibitory coupling due to (a) the Heaviside function based synapse; (b) the FTM coupling; (c) the α-dynamical synapse; and (d) the leech heart dynamical synapse. Color bar showing the maximal difference in the voltage values between the cells: zero for in-phase bursting and 0.08 for antiphase bursting. The parameters are $V_{\mathrm{K2}}^{\mathrm{shift}} = 0.02$, $I_{\mathrm{app}} = 0.006$, $\bar{g}_{\mathrm{Na}} = 160$, $\tau_{\mathrm{K2}} = 0.9$.

same multifunctional CPG, capable of switching between the two locomotor patterns with no change in the types or strengths of connections among the coupled neurons. At the neuronal level, crawling is governed by the command neurons firing in synchrony, whereas the CPG switches to the swimming rhythm when the neurons switch to antiphase bursting. The duty cycle of in-phase bursting, generating the crawling rhythm, is 7–10 times longer than that of the swimming rhythm [6]. The duty cycle is conjectured to be the main control parameter that determines the rhythms and can trigger the switching between the rhythms [36]. Our study of the spike interactions, the number and frequency of which are controlled by the duty cycle, together with previous studies of duty-cycle induced phase locking in larger inhibitory networks [11,12,35], promise to shed light on the genesis of switching mechanisms for emergent bursting patterns in real multifunctional CPGs and their realistic models.

APPENDIX: INDIVIDUAL NEURON MODELS

1. Leech heart interneuron model

This model including the fast sodium current I_{Na}, the slow potassium current I_{K2}, and an Ohmic leak current I_L is given by [10]

$$
\begin{aligned}
C\frac{dV}{dt} &= -I_{Na}(V) - I_{K2}(V) - I_L(V) - I_{app}, \\
I_{Na} &= \bar{g}_{Na}\, n^3\, h\, (V - E_{Na}), \quad n = n^\infty(V), \\
I_{K2} &= \bar{g}_{K2}\, m^2(V - E_K), \quad I_L = \bar{g}_L\,(V - E_L), \\
\tau_{Na}\frac{dh}{dt} &= h^\infty(V) - h, \quad \tau_{K2}\frac{dm}{dt} = m^\infty(V) - m.
\end{aligned}
\tag{A1}
$$

Here, V is the membrane potential, n and h are the gating variables for sodium channels, which activate and inactivate, respectively, as the membrane potential depolarizes: m is the gating variable for potassium channels that activate slowly as the membrane potential hyperpolarizes. The sodium current activates instantaneously. The time constants for the gating variables, maximum conductances and reversal potentials for all the channels and leak current, and the membrane capacitance are set as follows:

$$
\begin{aligned}
\tau_{Na} &= 0.0405 \text{ s}, \quad \bar{g}_{Na} = 200 \text{ nS}, \quad E_{Na} = 0.045 \text{ V}, \\
\tau_{K2} &= 0.25 \text{ s}, \quad \bar{g}_{K2} = 30 \text{ nS}, \quad E_K = -0.070 \text{ V}, \\
C &= 0.5 \text{ nF}, \quad \bar{g}_L = 8 \text{ nS}, \quad E_L = -0.046 \text{ V}.
\end{aligned}
$$

The steady state values of the gating variables are given by the following Boltzmann functions:

$$
\begin{aligned}
n^\infty(V) &= \{1 + \exp[-150(V + 0.0305)]\}^{-1}, \\
h^\infty(V) &= \{1 + \exp[500(V + 0.0333)]\}^{-1}, \\
m^\infty(V) &= \left\{1 + \exp\left[-83\left(V + 0.018 + V_{K2}^{shift}\right)\right]\right\}^{-1}.
\end{aligned}
$$

An applied current, $I_{app} = 0$ through the paper unless indicated otherwise (as in the quasi-strong coupling case, see Fig. 8). In this study, V_{K2}^{shift} is a primary bifurcation parameter that controls the number of spikes per burst.

2. Sherman model of pancreatic beta cells

This model [18] is based on two fast currents: calcium I_{Ca} and persistent potassium I_K, and a slow potassium current I_s. V is the membrane potential and m, n, and s are the voltage dependent gating variables for these currents. The model is given by the ODEs

$$
\begin{aligned}
\tau\frac{dV}{dt} &= -I_{Ca}(V) - I_K(V) - I_s(V), \\
I_{Ca} &= \bar{g}_{Ca}\, m^\infty(V)\,(V - E_{Ca}), \\
I_K &= \bar{g}_K\, n\,(V - E_K), \quad I_s = \bar{g}_s\, s\,(V - E_K), \\
\tau\frac{dn}{dt} &= \lambda[n^\infty(V) - n], \quad \tau_s\frac{ds}{dt} = s^\infty(V) - s.
\end{aligned}
\tag{A2}
$$

The governing equations for the gating variables n and s are similar to those in Eq. (A1), where the time constants, maximum conductances, and values of reversal potentials are set as follows:

$$
\begin{aligned}
\tau &= 0.02 \text{ s}, \quad \bar{g}_{Ca} = 3.6 \text{ nS}, \quad E_{Ca} = 0.025 \text{ V}, \\
\tau_s &= 5 \text{ s}, \quad \bar{g}_K = 10 \text{ nS}, \quad E_K = -0.075 \text{ V}, \\
\lambda &= 1, \quad \bar{g}_s = 4 \text{ nS}.
\end{aligned}
$$

In the model, an additional scaling factor λ controls the time scale of the persistent potassium channels. The steady state values of the gating variables are given by the Boltzmann functions

$$
\begin{aligned}
m^\infty(V) &= \{1 + \exp[-83.34(V + 0.02)]\}^{-1} \\
n^\infty(V) &= \{1 + \exp[-178.57(V + 0.016)]\}^{-1} \\
s^\infty(V) &= \{1 + \exp[-100(V + 0.035245)]\}^{-1}.
\end{aligned}
$$

3. Purkinje neuron model

This model [13] includes five currents: the sodium current I_{Na}, with slow inactivation h and fast instantaneous activation m^∞; the delayed rectifier potassium current I_K, with activation n; the noninactivating calcium current I_{Ca}, with activation c; the muscarinic receptor suppressed potassium current I_M, with activation M; the leak current I_L, and an applied current I_{app}. The individual cell model is given by

$$
\begin{aligned}
\frac{dV}{dt} &= -I_{Na}(V) - I_K(V) - I_{Ca}(V) - I_M(V) - I_L(V) - I_{app}, \\
I_{Na} &= \bar{g}_{Na}\, m^3\, h\,(V - E_{Na}), \quad m = m^\infty(V), \\
I_K &= \bar{g}_K\, n^4\,(V - E_K), \quad I_{Ca} = \bar{g}_{Ca}\, c^2(V - E_{Ca}), \\
I_M &= \bar{g}_M\, M\,(V - E_M), \quad I_L = \bar{g}_L\,(V - E_L).
\end{aligned}
\tag{A3}
$$

The governing equations for the gating variables h, n, c, and M are similar to those in Eq. (A1) where the values for maximum conductances and reversal potentials are set accordingly:

$$\bar{g}_{\mathrm{Na}} = 152 \text{ nS}, \quad E_{\mathrm{Na}} = 50 \text{ mV},$$
$$\bar{g}_{\mathrm{K}} = 10 \text{ nS}, \quad E_{\mathrm{K}} = -75 \text{ mV},$$
$$\bar{g}_{\mathrm{Ca}} = 1 \text{ nS}, \quad E_{\mathrm{Ca}} = 125 \text{ mV},$$
$$\bar{g}_{\mathrm{M}} = 0.75 \text{ nS}, \quad E_{\mathrm{M}} = -95 \text{ mV},$$
$$g_{\mathrm{L}} = 2 \text{ nS}, \quad E_{\mathrm{L}} = -70 \text{ mV}.$$

Voltage dependent time scales for the gating variables, measured in ms, and governed by the following functions:

$$\tau_{\mathrm{n}} = 0.25 + 4.35 \exp(-0.1|V + 10|),$$
$$\tau_{\mathrm{h}} = 0.15 + 1.15\{1 + \exp[0.0667(V + 33.5)]\}^{-1},$$
$$\tau_{\mathrm{c}} = [\alpha_{\mathrm{Ca}} + \beta_{\mathrm{Ca}}]^{-1}, \quad \tau_{\mathrm{M}} = [\alpha_{\mathrm{M}} + \beta_{\mathrm{M}}]^{-1},$$

where

$$\alpha_{\mathrm{Ca}} = 1.6/\{1 + \exp[-0.072(V - 5)]\},$$
$$\beta_{\mathrm{Ca}} = 0.02(V + 8.9)/\{-1 + \exp[0.2(V + 8.9)]\},$$
$$\alpha_{\mathrm{M}} = 0.02/\{1 + \exp[-0.2(V + 20)]\},$$
$$\beta_{\mathrm{M}} = 0.01 \exp[-0.0556(V + 43)].$$

The steady state values of the gating variables are given by the following Boltzmann functions:

$$n^{\infty}(V) = \{1 + \exp[-0.1(V + 29.5)]\}^{-1}$$
$$m^{\infty}(V) = \{1 + \exp[-0.1(V + 34.5)]\}^{-1}$$
$$h^{\infty}(V) = \{1 + \exp[0.0935(V + 59.4)]\}^{-1}$$
$$c^{\infty}(V) = \alpha_{\mathrm{Ca}}\tau_{\mathrm{c}}, \quad M^{\infty}(V) = \alpha_{\mathrm{M}}\tau_{\mathrm{M}}.$$

Here, the applied current is a bifurcation parameter, set for the cell to be a long burster, as $I_{\mathrm{app}} = -27$ nA.

[1] S. Phillips and Y. Takeda, Neurosci. Res. **65**, S192 (2009); U. Rutishauser, I. B. Ross, A. N. Mamelak, and E. M. Schuman, Nature (London) **464**, 903 (2010).

[2] N. Kopell and G. B. Ermentrout, in *Handbook of Dynamical Systems*, edited by B. Fiedler, Vol. 2 (Elsevier, Amsterdam, 2002), pp. 3–54.

[3] F. Skinner, N. Kopell, and E. Marder, J. Comput. Neurosci. **1**, 69 (1994); E. Marder and R. L. Calabrese, Physiol. Rev. **76**, 687 (1996).

[4] A. Prinz, D. Bucher, and E. Marder, Nat. Neurosci. **7**, 1345 (2004).

[5] T. G. Brown, Proc. R. Soc. London, Ser. B **84**, 308 (1911).

[6] K. L. Briggman and W. B. Kristan, Annu. Rev. Neurosci. **31**, 271 (2008).

[7] R. J. Calin-Jageman, M. J. Tunstall, B. D. Mensh, P. S. Katz, and W. N. Frost, J. Neurophysiol. **98**, 2382 (2007).

[8] J. Rinzel, in *Lecture Notes in Biomathematics*, Vol. 71 (Springer, Berlin, 1987), pp. 251–291; D. Terman, SIAM J. Appl. Math. **51**, 1418 (1991); R. Bertram, M. J. Butte, T. Kiemel, and A. Sherman, Bull. Math. Biol. **57**, 413 (1995); E. M. Izhikevich, Int. J. Bifurc. Chaos **10**, 1171 (2000); V. N. Belykh, I. V. Belykh, M. Colding-Joergensen, and E. Mosekilde, Eur. Phys. J. E **3**, 205 (2000); A. Shilnikov, R. L. Calabrese, and G. Cymbalyuk, Phys. Rev. E **71**, 056214 (2005); F. Frohlich and M. Bazhenov, *ibid.* **74**, 031922 (2006); A. L. Shilnikov and M. L. Kolomiets, Int. J. Bifurcation Chaos **18**, 2141 (2008).

[9] A. Shilnikov and G. Cymbalyuk, Phys. Rev. Lett. **94**, 048101 (2005).

[10] P. Channell, G. Cymbalyuk, and A. Shilnikov, Phys. Rev. Lett. **98**, 134101 (2007).

[11] I. Belykh and A. Shilnikov, Phys. Rev. Lett. **101**, 078102 (2008).

[12] A. Shilnikov, R. Gordon, and I. Belykh, Chaos **18**, 037120 (2008).

[13] M. A. Kramer, R. D. Traub, and N. J. Kopell, Phys. Rev. Lett. **101**, 068103 (2008).

[14] A. Shilnikov, Nonlinear Dynamics (2001), doi: 10.1007/s11071-011-0046-y.

[15] X.-J. Wang and J. Rinzel, Neural Comput. **4**, 84 (1992).

[16] C. van Vreeswijk, L. F. Abbott, and G. Bard Ermentrout, J. Comput. Neurosci. **1**, 313 (1994).

[17] D. Somers and N. Kopell, Biol. Cybern. **68**, 393 (1993); N. Kopell and D. Somers, J. Math. Biol. **33**, 261 (1995).

[18] A. Sherman, Bull. Math. Biol. **56**, 811 (1994).

[19] D. Golomb and J. Rinzel, Phys. Rev. E **48**, 4810 (1993); D. Terman, N. Kopell, and A. Bose, Physica D (Amsterdam) **117**, 241 (1998); R. C. Elson, A. I. Selverston, H. D. I. Abarbanel, and M. I. Rabinovich, J. Neurophysiol. **88**, 1166 (2002).

[20] J. Rubin and D. Terman, in *Handbook of Dynamical Systems*, edited by B. Fiedler, Vol. 2 (Elsevier, Amsterdam, 2002), pp. 93–148.

[21] J. Rubin and D. Terman, Neural Comput. **12**, 597 (2000).

[22] J. Rubin and D. Terman, SIAM J. Appl. Dyn. Sys. **1**, 146 (2002).

[23] T. Lewis and J. Rinzel, J. Comput. Neurosci. **14**, 283 (2003).

[24] N. Kopell and G. B. Ermentrout, Proc. Natl. Acad. Sci. USA **101**, 15482 (2004).

[25] R. C. Elson, A. I. Selverston, H. D. I. Abarbanel, and M. I. Rabinovich, J. Neurophysiol. **88**, 1166 (2002).

[26] M. Bazhenov, N. F. Rulkov, J.-M. Fellous, and I. Timofeev, Phys. Rev. E **72**, 041903 (2005); M. I. Rabinovich, P. Varona, A. I. Selverston, and H. D. I. Abarbanel, Rev. Mod. Phys. **78**, 1213 (2006).

[27] C. C. Canavier, D. A. Baxter, J. W. Clark, and J. H. Byrne, Biol. Cybern. **80**, 87 (1999).

[28] D. A. Baxter, H. A. Lechner, C. C. Canavier, R. J. Butera, A. A. Franceschi, J. W. Clark, and J. H. Byrne, in *Oscillations in Neural Systems*, edited by D. S. Levine, V. R. Brown, and V. T. Shirey (Lawrence Erlbaum Associates, Mahwah, New Jersey, 1999), pp. 51–78.

[29] E. M. Izhikevich, SIAM Rev. **43**, 315 (2001).

[30] V. E. Bondarenko, G. S. Cymbalyuk, G. Patel, S. P. DeWeerth, and R. L. Calabrese, Chaos **14**, 995 (2004).

[31] M. Dhamala, V. K. Jirsa, and M. Ding, Phys. Rev. Lett. **92**, 028101 (2004).

[32] T. Bem and J. Rinzel, J. Neurophysiol. **91**, 693 (2004).

[33] I. Belykh, E. de Lange, and M. Hasler, Phys. Rev. Lett. **94**, 188101 (2005).

[34] V. Matveev, A. Bose, and F. Nadim, J. Comput. Neurosci. **23**, 169 (2007).

[35] S. Jalil, I. Belykh, and A. Shilnikov, Phys. Rev. E **81**, 045201(R) (2010).

[36] J. Wojcik, R. Clewley, and A. Shilnikov, Phys. Rev. E **83**, 056209 (2011).

[37] G. S. Cymbalyuk, Q. Gaudry, M. A. Masino, and R. L. Calabrese, J. Neurosci. **22**, 10580 (2002).

[38] R. J. Calin-Jageman, M. J. Tunstall, B. D. Mensh, P. S. Katz, and W. N. Frost, J. Neurophysiol. **98**, 2382 (2007).

[39] W. E. Sherwood and J. Guckenheimer, SIAM J. Appl. Dyn. Sys. **9**, 659 (2010).